Scientific Research Publishing

Open Journal of Fluid Dynamics, 2024, 14, 147-162
https://www.scirp.org/journal/ojfd
ISSN Online: 2165-3860
ISSN Print: 2165-3852

Numerical Study of a Three-Dimensional Laminar Flow in a Rectangular Channel with a 180-Degree Sharp Turn

Takashi Yoshida

Department of Mechanical Systems Engineering, Shinshu University, Nagano, Japan
Email: t_yoshi@shinshu-u.ac.jp

How to cite this paper: Yoshida, T. (2024) Numerical Study of a Three-Dimensional Laminar Flow in a Rectangular Channel with a 180-Degree Sharp Turn. *Open Journal of Fluid Dynamics*, **14**, 147-162.
https://doi.org/10.4236/ojfd.2024.143007

Received: August 5, 2024
Accepted: September 8, 2024
Published: September 11, 2024

Abstract

This study presents a numerical analysis of three-dimensional steady laminar flow in a rectangular channel with a 180-degree sharp turn. The Navier-Stokes equations are solved by using finite difference method for Re = 900. Three-dimensional streamlines and limiting streamlines on wall surface are used to analyze the three-dimensional flow characteristics. Topological theory is applied to limiting streamlines on inner walls of the channel and two-dimensional streamlines at several cross sections. It is also shown that the flow impinges on the end wall of turn and the secondary flow is induced by the curvature in the sharp turn.

Keywords

180-Degree Sharp Turn Channel, Three Dimensional Steady Flow, Limiting Streamline, Topological Theory

1. Introduction

A sharp turn channel is a U-shaped two-way channel with a rectangular cross section that features a 180-degree turn. Industrially, it has been used in various heat exchangers, including the cooling channels in gas turbine blades. Recently, it has been used in separator channels in fuel cells. Sharp turn channels are practically used across a wide range of Reynolds numbers, from laminar to turbulent flow, making it important to clarify the detailed flow field in the channel. This understanding will lead to the miniaturization and high performance of various energy devices, as well as the reduction of environmental impact, and will enable the development of new devices.

A characteristic of the flow in a sharp turn channel is that, although the chan-

nel shape is simple, the flow becomes complex and three-dimensional. In the turn section, a first-kind secondary flow occurs due to an imbalance of forces caused by centrifugal force and pressure gradient. Additionally, because of the sharp bend in the turn section, the main flow collides with the wall, branching out in all directions and further complicating the secondary flow. Furthermore, separation and reattachment at the turn corners and baffle tips lead to phenomena such as separation bubbles and vortex shedding.

Many experimental studies have been conducted on sharp-turn channels. Metzger *et al.* [1] measured the pressure distribution in the channel to determine the pressure loss and visualized the surface streamlines on the channel walls. Liou and Chen [2] used Laser Doppler Velocimetry to measure the flow within rotating sharp turn channels, examining the characteristics of the complex flow in the turn section and the influence of Coriolis forces based on mean velocity and turbulence intensity. Liou and Chen [3] conducted visualization and measured temperature distribution using thermocouples to investigate the secondary flow in the turn section and the variation of the Nusselt number in the flow direction. Astarita and Cardone [4] measured the heat transfer coefficient within the channel using infrared thermography to investigate the effect of Reynolds number on heat transfer. Martin *et al.* [5] used Particle Image Velocimetry (PIV) to measure the low Reynolds number flows in a sharp turn channel in a fuel cell and investigated the vector field in two-dimensional cross-sections. Yoon *et al.* [6] also measured the flow within sharp turn channels in fuel cells using PIV. Gallo and Astarita [7] measured the flow within rotating sharp turn channels using PIV, studying the impact of rotation on the distribution of secondary flow and vorticity in the mean velocity field. Furthermore, Gallo *et al.* [8] measured the temperature field in the same flow field using thermography and investigated the effect of rotation on heat transfer. Wang *et al.* [9] measured heat transfer and pressure loss in sharp turn channels with smooth and ribbed walls, investigating the effect of ribs on enhancing heat transfer. Zhao *et al.* [10]-[12] installed three types of vortex generators on the endwall of a sharp turn channel to enhance heat transfer.

These experimental studies have revealed the velocity fields in several cross-sections perpendicular to the channel axis and the symmetric plane of the channel, as well as the heat transfer characteristics of the channel walls. Liou and Chen [2] presented vector plots of the flow patterns in the symmetric plane of the channel and the cross-stream secondary flow patterns inside the turn using LDV measurements. Martin *et al.* [5] provided distributions of instantaneous flow velocity, out-of-plane vorticity, streamline patterns, and velocity magnitude in both the streamwise and cross-flow planes using PIV measurements. Yoon *et al.* [6] demonstrated the ensemble-averaged velocity field in the symmetric plane of a 180-degree switchback. However, it is difficult to measure three-dimensional velocity fields and velocity fields near the walls, which are important for heat transfer and the flow patterns near the walls of the turn section. The complex three-dimensional flow field structure in a sharp turn channel remains unclear.

Numerical studies have also been conducted. Hwang and Lai [13] performed calculations of three-dimensional steady laminar flow in a rotating sharp turn channel. The Reynolds numbers were 300, 500, and 1000, and all were steady flows. They investigated the axial velocity distribution, secondary flow vector, wall friction coefficient, and pressure loss, but did not investigate the detailed changes in the patterns of the three-dimensional flow near the wall or the secondary flow in the turns. Yoon *et al.* [6] performed steady numerical calculations of the flow in a sharp turn channel in a fuel cell for a Reynolds number of 400 and compared the results with PIV results. Chung *et al.* [14] performed two-dimensional numerical calculations of sharp turn channels. They performed calculations for Reynolds numbers below 1000 and reported that when the Reynolds number was above 600, the flow field became unsteady and heat transfer after the turn increased due to the mixing effect of the unsteady separated vortex. Zhang and Pothérat [15] performed calculations of two-dimensional sharp turn channels similar to those by Chung *et al.* [14]. They performed calculations for Reynolds numbers ranging from 1 to 2500 and turn clearances ranging from 0.1 to 10. When the turn clearance was 1, their calculations also showed that the flow became unsteady at Reynolds numbers above 700. Zhang and Pothérat reported that in two-dimensional sharp turn channels, the separated vortex in the wake of the turn becomes unsteady at low Reynolds numbers due to Kelvin-Helmholtz instability. Calculations of high Reynolds number turbulent flow fields have also been performed as part of fundamental research into cooling passages in gas turbines. Sugiyama *et al.* [16] calculated the high Reynolds number turbulent flow field in a sharp turn passage with ribs using an algebraic stress model and reported that the mean velocity and secondary flow vectors qualitatively agreed with the experimental values. Shen *et al.* [17] investigated the flow and heat transfer in a sharp turn channel with ribs and dimples using the *k*-w SST turbulence model. Erelli *et al.* [18] calculated high Reynolds number flows with different turn geometries using a realizable *k*-ε model. Even in these numerical studies, the details of the flow field near the turn wall and the three-dimensional flow structure have not been fully elucidated.

It is not easy to investigate the structure of a complex three-dimensional flow field such as that in a sharp turn channel. Hunt *et al.* [19] demonstrated that considering limiting streamlines on the surface of an object and streamlines in cross sections through the flow field is effective for investigating three-dimensional flow fields. Hunt *et al.* demonstrated that analyzing the limiting streamlines on object surfaces and the streamlines within cross-sections of the flow field is effective for studying three-dimensional flow fields. They analyzed two-dimensional equilibrium points appearing on limiting streamlines and cross-sectional streamlines, deriving relationships for the types and numbers of equilibrium points known as topological rules. The usefulness of two-dimensional equilibrium points and their topology in the analysis of three-dimensional flows has been reviewed by Tobak and Peake [20], Perry and Chong [21], and Déley [22] [23]. As reviewed by Déley [23], analysis of three-dimensional separated flows using

two-dimensional topology has been performed on the flow field around objects. For example, Liakos and Malamataris [24] investigated the structure of separation and reattachment through the two-dimensional topology of equilibrium points on limiting streamlines on a wall around a cube on a flat plate. In contrast, there has been no research applying topology analysis to three-dimensional separation and reattachment in a channel. This study considers analyzing two-dimensional equilibrium points and topologies as an effective approach to elucidate the complex three-dimensional flow field in a sharp turn channel.

In this study, a three-dimensional numerical analysis is performed on the velocity field in a sharp turn channel. Calculations are conducted for a steady laminar flow with a Reynolds number of 900. Limiting streamlines obtained from the wall friction stress vector and two-dimensional streamlines in the channel cross-section are visualized, and the three-dimensional structure of the flow field is investigated from the streamline pattern and the topology of two-dimensional equilibrium points. The flow field in the channel is also examined by visualizing three-dimensional streamlines that track the movement of fluid particles.

2. Flow Field Configuration and Numerical Method

2.1. Flow Field Configuration

Figure 1 shows a schematic diagram of the sharp turn channel and the calculation domain. The channel shape is the same as the experimental device used by Syuhada *et al.* [25]. The channel cross-section is a rectangle with an aspect ratio of 2:1, with the hydraulic diameter of the channel cross-section as its representative length, the straight section length being 10, the partition thickness being 0.3, and the turn gap being 1.5. The names of each wall surface in the channel are shown in Figure 1.

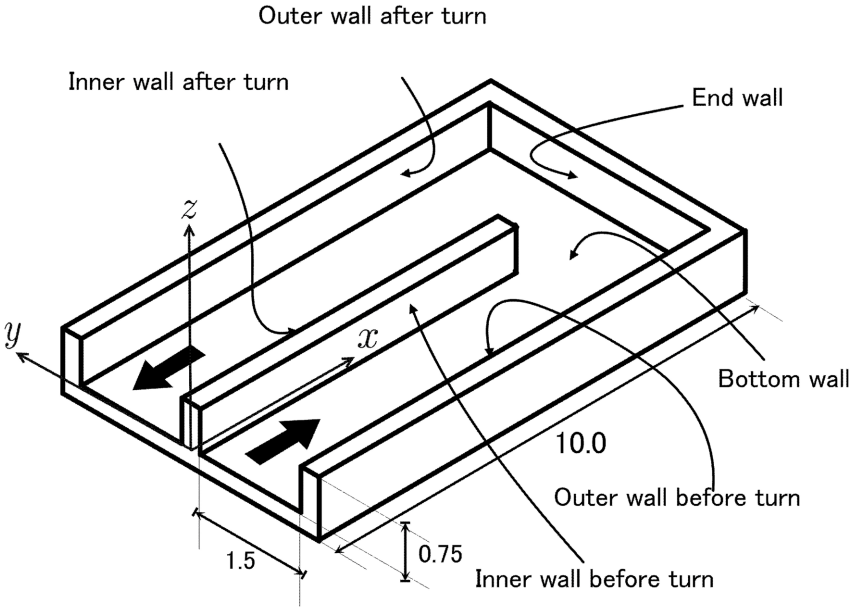

Figure 1. Schematic of the three-dimensional channel with a 180-degree sharp turn.

2.2. Numerical Method

The governing equations are the three-dimensional unsteady incompressible Navier-Stokes equations non-dimensionalized by the cross-sectional hydraulic diameter of the channel, and the equation of continuity,

$$\frac{\partial \boldsymbol{u}}{\partial t}+\left(\boldsymbol{u}\cdot\nabla\right)\boldsymbol{u}=-\nabla p+\frac{1}{Re}\nabla^2\boldsymbol{u}\,, \tag{1}$$

$$\nabla\cdot\boldsymbol{u}=0\,. \tag{2}$$

Discretization was performed using the finite difference method. The convective term of Equation (1) was discretized with a third-order upwind difference scheme, while other terms of Equation (1) were discretized with a second-order central difference scheme. The computational grid employed non-uniform staggered grids in the *x*, *y*, and *z* directions. Time integration of Equation (1) used the first-order implicit splitting method of Dukowicz and Dvinsky [26]. The pressure Poisson equation resulting from the splitting of the Navier-Stokes equations was solved using the BiCGSTAB method. The maximum residual of the discretized continuity Equation (2) across all grid points was less than 10^{-8}, indicating that the continuity error in the computed velocity field is sufficiently small and that the computed values met the incompressibility condition adequately. The velocity inlet condition provided a fully developed laminar flow solution for a rectangular straight duct. Calculations were performed for three Reynolds numbers, Re = 200, 500, and 900, with all calculations converging to a steady-state. The steady-state results for Re = 900 were consistent with those of Hwang and Lai [13]. This paper presents the results for Re = 900.

2.3. Visualization Methods

In this study, the limiting streamlines on the wall, the streamlines in a two-dimensional cross section, and the three-dimensional streamlines are visualized. The limiting streamlines are the curves formed by the shear stress vectors on the wall surface. For example, considering the bottom wall in **Figure 1**, the shear stress vector τ_s on the bottom wall is

$$\tau_s=\left(\mu\frac{\partial u}{\partial z},\mu\frac{\partial v}{\partial z}\right)_{z=0}\equiv\left(\mu\alpha,\mu\beta\right). \tag{3}$$

The vector line of τ_s becomes a differential equation for a streamline if t is used the parameters that represent the points on the curve,

$$\frac{\mathrm{d}x}{\mathrm{d}t}=\mu\alpha,\quad\frac{\mathrm{d}y}{\mathrm{d}t}=\mu\beta\,, \tag{4}$$

$$\frac{\mathrm{d}x}{\alpha}=\frac{\mathrm{d}y}{\beta}\,. \tag{5}$$

The curve defined by Equation (5) is the limiting streamline. In the experiment, it is equivalent to the oil film method, which involves applying oil or paint to the surface of the object to visualize the flow patterns on the surface. In this study, the shear stress vector field was calculated on the wall surface using a fi-

nite difference scheme obtained by applying a first-order accurate one-sided difference to Equation (3). Limiting streamlines were drawn from this vector field using MATLAB's graphics function streamline. For two-dimensional cross-sectional streamlines, cross-sectional streamlines were drawn using MATLAB's streamslice, which draws streamlines within an arbitrary cross section from a three-dimensional velocity vector field. For three-dimensional streamlines, three-dimensional streamlines were visualized using MATLAB's streamtube.

3. Numerical Results

3.1. The Topology of Flow and Tree-Dimensional Fow Field

The flow structure near the wall is represented by limiting streamlines and their topology. The solution trajectories around equilibrium points in a two-dimensional linear dynamical system can be classified by the complex eigenvalues of the coefficient matrix in the motion equation of the dynamical system [19] [22] [23]. Figure 2 shows the representative topologies of solution curves around equilibrium points. Equilibrium points are classified into saddle point and nodal point, with nodal point further classified into node and focus. Additionally, based on the real parts of the eigenvalues, they can be divided into stable and unstable. Stable point represents the separation point of the flow field, while unstable point represents the attachment point of the flow field [21] [25].

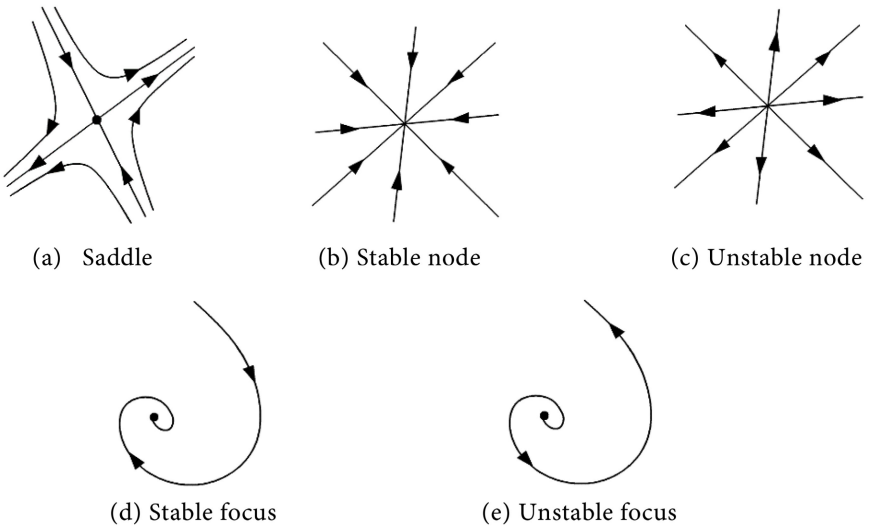

Figure 2. Classification of singular points.

Figure 3 shows the limiting streamlines of the sharp turn section as viewed from both the upstream and downstream sides of the turn. Figure 4 presents the limiting streamlines on the four walls of the turn section, unfolded and plotted with equilibrium points. The equilibrium points are identified by comparing the pattern of limiting streamlines in Figure 4 with the classifications in Figure 2. On the upstream outer wall of the turn in the lower part of Figure 4, there is a U-shaped separation line indicated by ①, and at the tip of the U-shape, ②, a

saddle point of the separation point is formed. The separation nature of the saddle point at ② is described by Déley [23]. On the end face in the right part of Figure 4, the flow in the central part of the upstream z direction collides with the end face, forming an unstable node at the stagnation point ③. According to Déley [23], an unstable node is a point where the flow collides with the surface of the object. The separation region formed by the stagnation point on this end face and the upstream corner of the turn becomes the separation bubble region in the corner part. Inside the separation bubble on the end face, there is one saddle point at ④ and two stable foci at ⑤. According to Déley [23], stable focus corresponds to a vortex structure, and according to Hunt *et al.* [19], such points indicate separation. Inside the separation bubble on the upstream outer wall of the turn, three unstable nodes and two saddles at ⑥ are formed, resulting in a complex attachment flow. On the downstream outer wall of the turn in the upper part of Figure 4, an unstable node at the stagnation point ⑦ is formed by the collision of the flow at the z center. On the lower wall in the central part of Figure 4, limiting streamlines converge from the outer wall of the turn and the end face of the turn to the tip of the downstream partition wall of the turn. At the center of the concentration of streamlines, ⑧, a stable focus is formed, indicating the presence of a vortex structure.

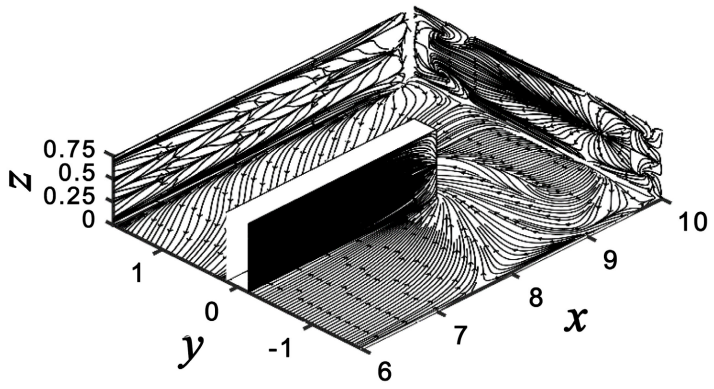

(a) Oblique view from upstream side.

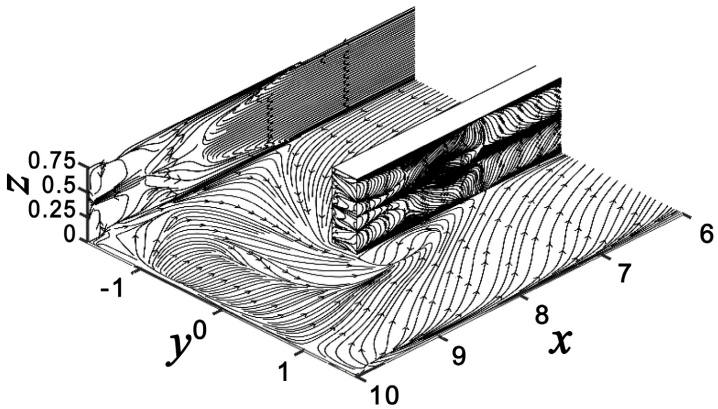

(b) Oblique view from downstream side.

Figure 3. Limiting streamlines on walls of the 180-degree sharp turn channel.

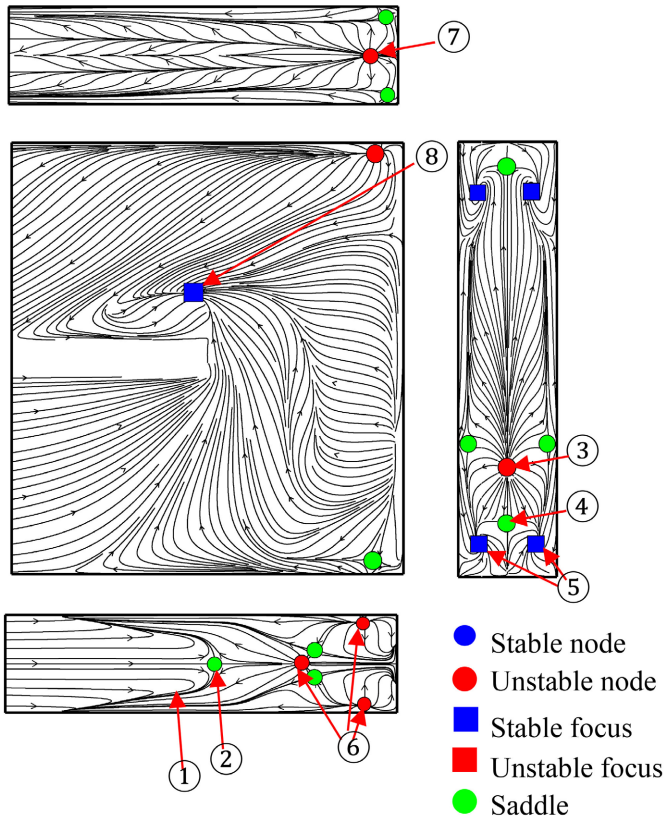

Figure 4. Limiting streamlines and critical points on walls of the sharp turn channel.

The three-dimensional structure of the flow inside the sharp turn channel is illustrated by streamlines in cross-sections perpendicular to the z-axis and three-dimensional streamlines. The straight part upstream of the turn is a fully developed laminar solution in a rectangular straight pipe, so the streamlines are straight. To show the detailed streamline shapes in the turn section, the cross-sectional streamlines, three-dimensional streamlines, and limiting streamlines all start from $x = 7.0$. Additionally, to indicate differences in height direction, the starting points of the cross-sectional and three-dimensional streamlines are chosen at four different heights in the z-direction, ranging from near the lower wall at $z = 0.05$ to near the center of the channel at $z = 0.36$. Figure 5(a) shows the cross-sectional streamlines (red lines) at $z = 0.05$ near the lower wall, and Figure 5(b) shows the three-dimensional streamlines starting from $x = 7.0$, $z = 0.05$. The color of the three-dimensional streamlines corresponds to the height in the z-coordinate. The three-dimensional streamlines near the lower wall flow through the central part of the channel up to the front of the turn section. Figure 6 shows the cross-sectional and three-dimensional streamlines at $z = 0.12$. The cross-sectional streamlines flow along the turn without colliding with the end face or outer wall. Vortex structures can be observed in the separation region of the upstream corner of the turn and the separation region at the tip of the partition wall. The three-dimensional streamlines follow the cross-sectional streamlines upstream of the turn but flow near the center of the channel in a spiral pattern

from the turn section. Figure 7 shows the cross-sectional and three-dimensional streamlines at $z = 0.24$. The cross-sectional streamlines collide with the end face and the downstream wall of the turn, forming separation circulation vortices at the upstream corner of the turn and the tip of the partition wall. The three-dimensional streamlines form a larger helical secondary flow structure than the streamlines at $z = 0.24$ in the turn section and do not flow into the separation vortex region indicated by the cross-sectional streamlines. Figure 8 shows the cross-sectional and three-dimensional streamlines near the center height of the channel at $z = 0.36$. The cross-sectional streamlines collide with the end face, forming an unstable node at the stagnation point. The collided flow then flows along the end face, colliding again near the corner of the downstream wall of the turn to form another unstable node at the stagnation point. The three-dimensional streamlines flow along the cross-sectional streamlines until they collide with the end face and the downstream wall of the turn. After the collision, they flow into the separation vortex region at the corner, then further along the lower wall, passing through the separation vortex region on the downstream side of the partition wall, and continuing downstream.

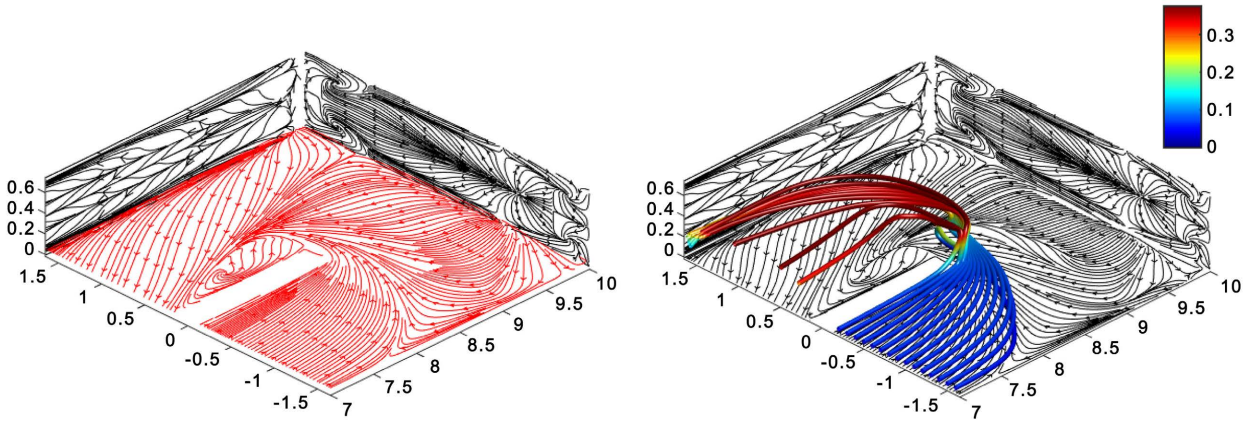

(a) Stremalines on z=0.05 section. (b) 3D streamlines stared x=7.0 z=0.05.

Figure 5. Limiting streamlines on walls and streamlines on $z = 0.05$.

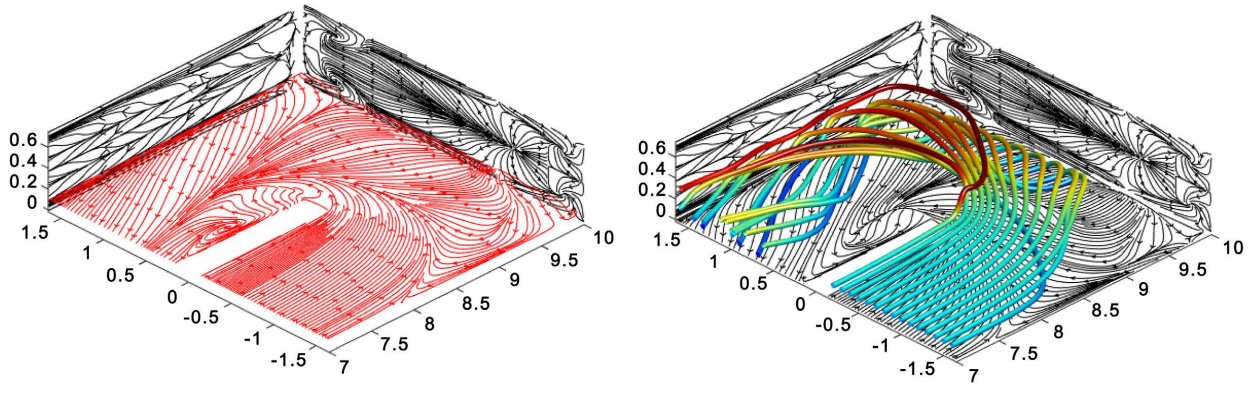

(a) Stremalines on z=0.12 section. (b) 3D streamlines stared x=7.0 z=0.12.

Figure 6. Limiting streamlines on walls and streamlines on $z = 0.12$.

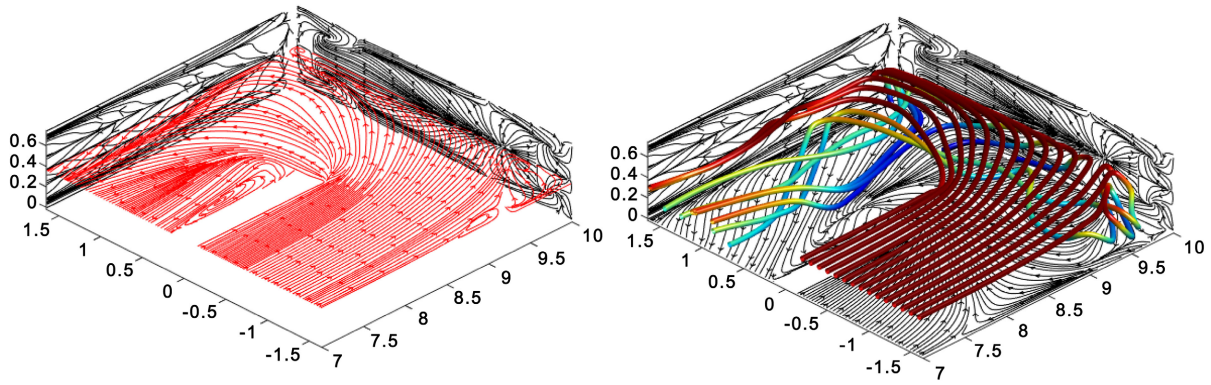

(a) Stremalines on z=0.24 section. (b) 3D streamlines stared x=7.0 z=0.24.

Figure 7. Limiting streamlines on walls and streamlines on z = 0.24.

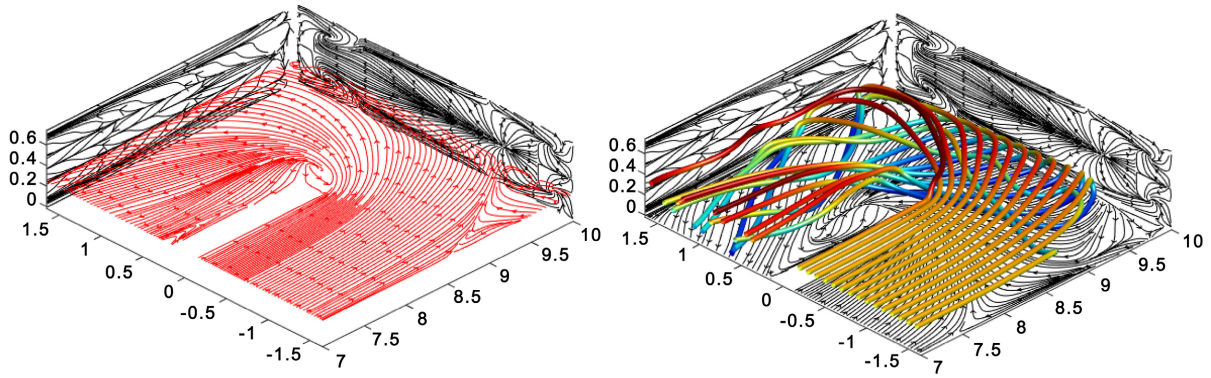

(a) Stremalines on z=0.36 section. (b) 3D streamlines stared x=7.0 z=0.36.

Figure 8. Limiting streamlines on walls and streamlines on z = 0.36.

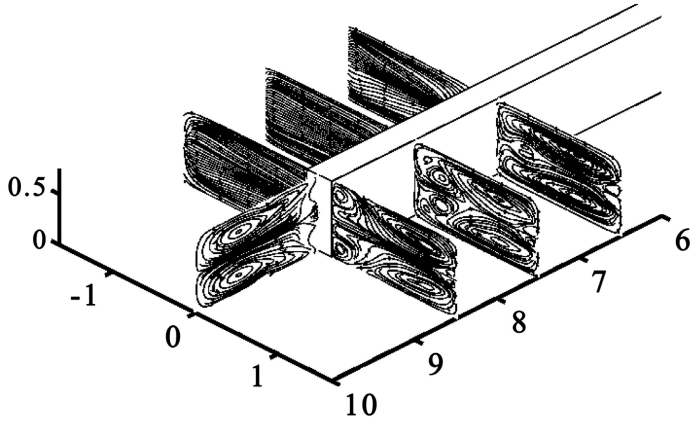

Figure 9. Secondary flow streamlines in the channel.

3.2. The Topology of Secondary Flow

Figure 9 shows the changes in secondary flow from upstream to downstream as streamlines in cross-sections perpendicular to the main flow. Figure 10 displays the cross-sectional streamlines and equilibrium point distribution for each face taken from the center of the turn section to the downstream part of the turn

shown in Figure 9. From the center of the turn in Figure 9 ($y = 0$ cross-section), a symmetric rotational component not observed in the upstream cross-sections appears, indicating the generation of secondary flow. There is a large vortex of secondary flow on the outer wall side, and a vortex rotating in the opposite direction to the secondary flow appears inside the separation bubble on the partition wall side. However, after passing through the separation bubble region, the vortex on the partition wall side gradually disappears, forming a large, symmetric vortex.

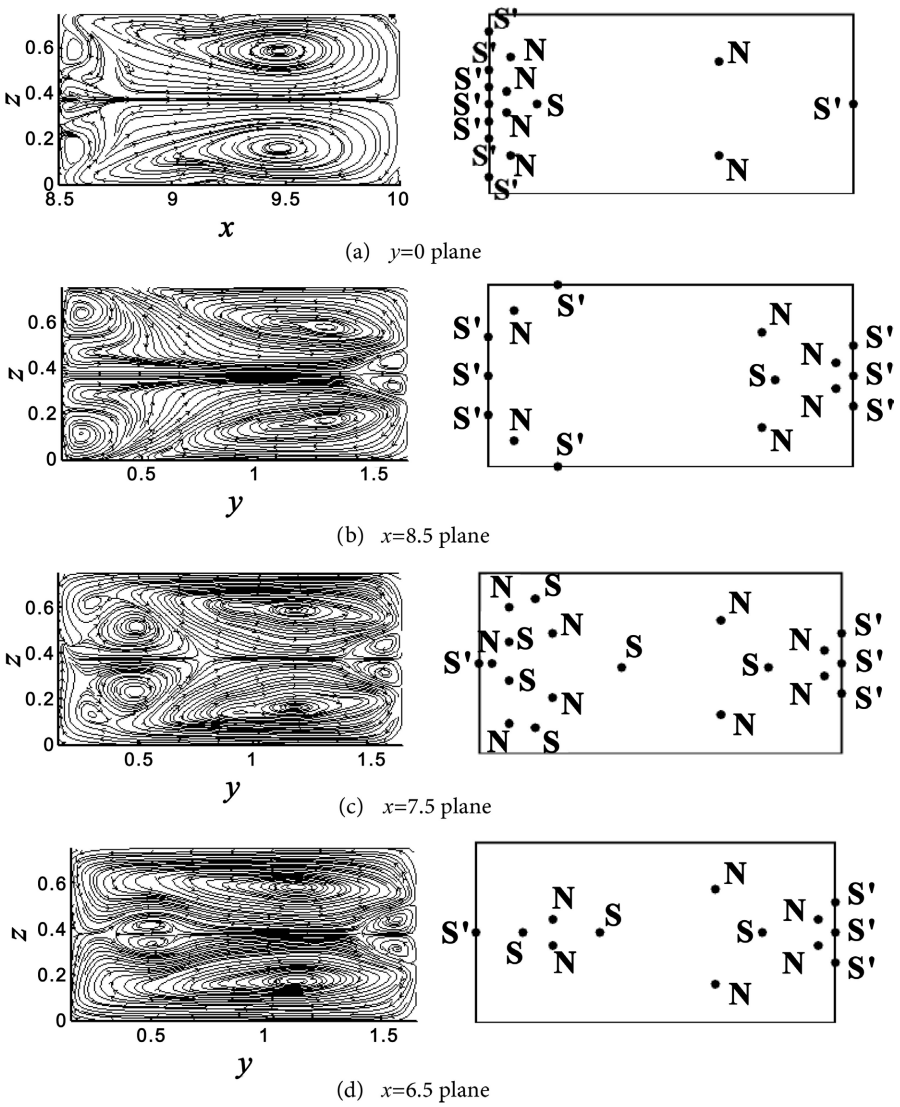

(a) y=0 plane

(b) x=8.5 plane

(c) x=7.5 plane

(d) x=6.5 plane

Figure 10. Secondary flow streamlines in the channel.

The topological rules derived by Hunt *et al.* [19] are applied to these cross-sectional streamlines. Hunt *et al.* introduced additional equilibrium points on solid surfaces, which are half the shape of nodes and saddle points, naming them half-node and half-saddle. They derived a relationship equation for the number of these equilibrium points in cross-sectional streamlines

$$\left(\sum_N + \frac{1}{2}\sum_{N'}\right) - \left(\sum_S + \frac{1}{2}\sum_{S'}\right) = 1 - n. \quad (7)$$

Here, N represents node, S represents saddle, N' represents half-node, and S' represents half-saddle. In Equation (7), $\sum_N$ and $\sum_S$ denote the total numbers of nodes and saddles, respectively, while $\sum_{N'}$ and $\sum_{S'}$ denote the total numbers of half-nodes and half-saddles. n represents the connectivity of the space. Sheu and Tsai [27] computed the topological rules of Equation (7) for three-dimensional closed cavity cross-sectional streamlines and demonstrated that it results in Equation (8),

$$\left(\sum_N + \frac{1}{2}\sum_{N'}\right) - \left(\sum_S + \frac{1}{2}\sum_{S'}\right) = 1 \quad (8)$$

Here, $n = 0$ because any cross-section within a closed cavity is a simply connected space without holes or objects, according to Déley [23]. Similarly, we compute the topological rules for the vertical cross-sections downstream of the sharp turn channel. Since there are no holes or objects in the vertical cross-sections of the sharp turn channel, $n = 0$, and the results should match Equation (8) obtained by Sheu and Tsai. The right column of **Figure 10** shows the distribution of equilibrium points for each cross-section. The equilibrium points were identified from the local patterns of the streamlines in the left column of **Figure 10**. For the $y = 0$ cross-section in **Figure 10(a)**, we have $\sum_N = 6$, $\sum_{N'} = 0$, $\sum_S = 1$, $\sum_{S'} = 8$ resulting in Equation (7) = 1. For the $x = 8.5$ cross-section in **Figure 10(b)**, we have $\sum_N = 6$, $\sum_{N'} = 0$, $\sum_S = 1$, $\sum_{S'} = 8$ resulting in Equation (7) = 1. For the $x = 7.5$ cross-section in **Figure 10(c)**, we have $\sum_N = 9$, $\sum_{N'} = 0$, $\sum_S = 6$, $\sum_{S'} = 4$ resulting in Equation (7) = 1. For the $x = 6.5$ cross-section in **Figure 10(d)**, we have $\sum_N = 6$, $\sum_{N'} = 0$, $\sum_S = 3$, $\sum_{S'} = 4$ resulting in Equation (7) = 1. Thus, the results obtained for all cross-sections are consistent with the value obtained from Equation (8) by Sheu and Tsai.

3.3. Secondary Flow

The Prandtl's first-kind of secondary flow which occurs in a smoothly curved circular pipe, arises from the imbalance between the pressure gradient and centrifugal force due to the curvature of the channel, as studied by Chin *et al.* [28]. In a sharp turn channel with its abrupt 180-degree bend, this behavior is expected to differ from that in a generally smooth curved pipe. Despite numerous experimental and numerical studies mentioned in the introduction, no explicit study has detailed the relationship between the pressure gradient and streamlines in the sharp turn section. Thus, **Figure 11** overlays the streamlines, depicted with black solid lines, and the pressure gradient vectors, depicted with blue arrows, in the cross-section. The pressure gradient vectors were computed using the gradient function in MATLAB from pressure values and plotted with the quiver function. **Figure 11(a)** shows the cross-section near the lower wall ($z =$

0.05), while Figure 11(b) shows the cross-section at the center of the channel (z = 0.36). The pressure gradient vectors are almost the same regardless of z, but the direction of the streamlines varies significantly with z. In the center of the channel, the pressure gradient vectors and streamlines are nearly orthogonal across the entire turn section and point towards the direction of the partition wall's tip. Unlike smooth curved pipes, the sharp turn's pressure field is influenced by the large bending of the flow field due to the high-speed flow in the channel center colliding with the end face and downstream outer wall. On the other hand, near the wall surfaces, the lower velocity due to viscosity results in smaller centrifugal forces, so the flow is more influenced by the pressure gradient. Consequently, near the lower wall, the direction of the pressure gradient vectors aligns closely with the direction of the limiting streamlines, flowing from the end face and outer wall towards the partition wall. While the pressure field has almost the same gradient regardless of z, the direction of the streamlines differs greatly between the central region of the channel and near the walls, indicating significant effects of flow curvature due to collisions.

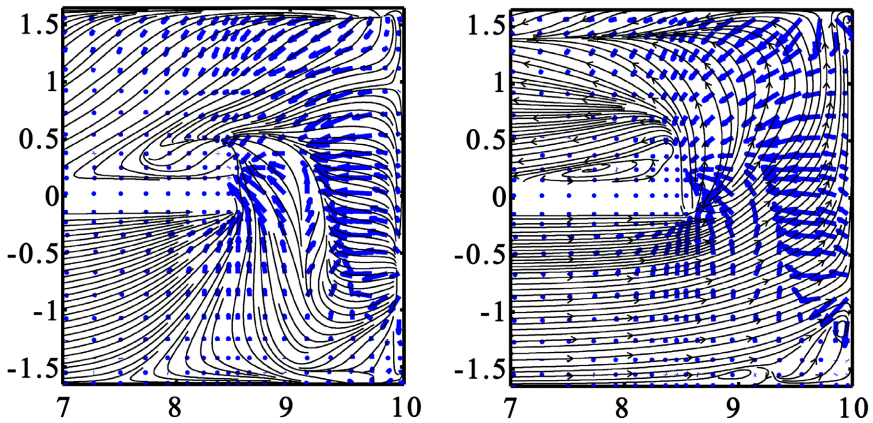

Figure 11. Streamlines and pressure gradient vector.

4. Conclusions

Three-dimensional numerical analysis was conducted on the velocity field within the sharp turn channel, archiving a steady-state solution at a Reynolds number of 900. Limiting streamlines, two-dimensional streamlines within cross-sections, and three-dimensional streamlines were visualized to investigate the three-dimensional structure of the flow field. The flow, initially steady in the upstream straight section, becomes complex and three-dimensional as it traverses the turn section. Near the central cross-section, the flow collides with the end face and downstream outer wall, forming nodes. The flow then spirals downstream along the lower wall due to secondary flow effects. At the turn's corner, a circulation region is created, which then continues downstream. Near the upper and lower walls, the flow aligns closely with the wall surfaces until it reaches the turn section, where it flows near the partition wall and subsequently into the main flow

or the circulation region at the downstream partition wall tip.

The topological rules derived by Hunt *et al*. [19] were applied to the streamlines in cross-sections perpendicular to the main flow. The application of these rules confirmed that the relationship given in Equation (7) for the numbers of nodes, saddles, half-nodes, and half-saddles consistently resulted in the value of 1 for all cross-sections. This finding verifies that the topological rules are applicable to simply connected two-dimensional cross-sectional areas bounded by walls. The topology analysis of the streamlined pattern in a sharp turn channel is a novel research approach that can be applied to analyzing flow in the serpentine channel of a fuel cell. The secondary flow was analyzed based on streamlines and pressure gradient vectors in the x-y cross-section. It was demonstrated that the pressure field within the turn section results from high-speed flow in the channel center colliding with the end face and downstream outer wall, which induces significant bending. Conversely, the slower flow near the wall surfaces aligns with the pressure gradient, leading to the formation of secondary flow.

Conflicts of Interest

The author declares no conflicts of interest regarding the publication of this paper.

References

[1] Metzger, D.E., Plevich, C.W. and Fan, C.S. (1984) Pressure Loss through Sharp 180 Deg Turns in Smooth Rectangular Channels. *Journal of Engineering for Gas Turbines and Power*, **106**, 677-681. https://doi.org/10.1115/1.3239623

[2] Liou, T.M. and Chen, C.C. (1999) LDV Study of Developing Flows through a Smooth Duct with a 180 Deg Straight-Corner Turn. *Journal of Turbomachinery*, **121**, 167-174. https://doi.org/10.1115/1.2841228

[3] Liou, T.M. and Chen, C.C. (1999) Heat Transfer in a Rotating Two-Pass Smooth Passage with a 180° Rectangular Turn. *International Journal of Heat and Mass Transfer*, **42**, 231-247. https://doi.org/10.1016/s0017-9310(98)00148-3

[4] Astarita, T. and Cardone, G. (2000) Thermofluidynamic Analysis of the Flow in a Sharp 180° Turn Channel. *Experimental Thermal and Fluid Science*, **20**, 188-200. https://doi.org/10.1016/s0894-1777(99)00045-x

[5] Martin, J., Oshkai, P. and Djilali, N. (2004) Flow Structures in a U-Shaped Fuel Cell Flow Channel: Quantitative Visualization Using Particle Image Velocimetry. *Journal of Fuel Cell Science and Technology*, **2**, 70-80. https://doi.org/10.1115/1.1843121

[6] Yoon, S.Y., Ross, J.W., Mench, M.M. and Sharp, K.V. (2006) Gas-phase Particle Image Velocimetry (PIV) for Application to the Design of Fuel Cell Reactant Flow Channels. *Journal of Power Sources*, **160**, 1017-1025. https://doi.org/10.1016/j.jpowsour.2006.02.043

[7] Gallo, M. and Astarita, T. (2009) 3D Reconstruction of the Flow and Vortical Field in a Rotating Sharp "U" Turn Channel. *Experiments in Fluids*, **48**, 967-982. https://doi.org/10.1007/s00348-009-0776-5

[8] Gallo, M., Astarita, T. and Carlomagno, G.M. (2012) Thermo-Fluid-Dynamic Analysis of the Flow in a Rotating Channel with a Sharp "U" Turn. *Experiments in Fluids*, **53**, 201-219. https://doi.org/10.1007/s00348-012-1283-7

[9] Wang, C., Wang, L. and Sundén, B. (2015) Heat Transfer and Pressure Drop in a Smooth and Ribbed Turn Region of a Two-Pass Channel. *Applied Thermal Engineering*, **85**, 225-233. https://doi.org/10.1016/j.applthermaleng.2015.03.079

[10] Zhao, Z., Luo, L., Du, W., Wang, S., Zhou, X. and Sundén, B. (2022) Experimental Study on the Augmented Nusselt Number of the Endwall through a Square-Sectioned Sharp-Turn Channel Using Novel Heat Exchanger. *International Journal of Heat and Mass Transfer*, **192**, Article ID: 122920. https://doi.org/10.1016/j.ijheatmasstransfer.2022.122920

[11] Zhao, Z., Luo, L., Zhou, X., Wang, S., Wang, Z. and Sundén, B. (2022) Analysis of Enhanced Turbulent Heat Transfer in a Sharp Turn Channel Having Novel Designed Endwall with Longitudinal Vortex Generator. *International Communications in Heat and Mass Transfer*, **131**, Article ID: 105874. https://doi.org/10.1016/j.icheatmasstransfer.2021.105874

[12] Zhao, Z., Luo, L., Qiu, D., Zhou, X., Wang, Z. and Sundén, B. (2022) Experimental Evaluation of Longitudinal and Transverse Vortex Generators on the Endwall of a Serpentine Passage. *International Journal of Thermal Sciences*, **176**, Article ID: 107521. https://doi.org/10.1016/j.ijthermalsci.2022.107521

[13] Hwang, J. and Lai, D. (1998) Three-Dimensional Laminar Flow in a Rotating Multiple-Pass Square Channel with Sharp 180-Deg Turns. *Journal of Fluids Engineering*, **120**, 488-495. https://doi.org/10.1115/1.2820689

[14] Chung, Y.M., Tucker, P.G. and Roychowdhury, D.G. (2003) Unsteady Laminar Flow and Convective Heat Transfer in a Sharp 180° Bend. *International Journal of Heat and Fluid Flow*, **24**, 67-76. https://doi.org/10.1016/s0142-727x(02)00202-3

[15] Zhang, L. and Pothérat, A. (2013) Influence of the Geometry on the Two- and Three-Dimensional Dynamics of the Flow in a 180° Sharp Bend. *Physics of Fluids*, **25**, Article ID: 053605. https://doi.org/10.1063/1.4807070

[16] Sugiyama, H., Tanaka, T. and Mukai, H. (2007) Numerical Analysis of Turbulent Flow Separation in a Rectangular Duct with a Sharp 180-degree Turn by Algebraic Reynolds Stress Model. *International Journal for Numerical Methods in Fluids*, **56**, 2207-2228. https://doi.org/10.1002/fld.1581

[17] Shen, Z., Xie, Y. and Zhang, D. (2015) Numerical Predictions on Fluid Flow and Heat Transfer in U-Shaped Channel with the Combination of Ribs, Dimples and Protrusions under Rotational Effects. *International Journal of Heat and Mass Transfer*, **80**, 494-512. https://doi.org/10.1016/j.ijheatmasstransfer.2014.09.057

[18] Erelli, R., Saha, A.K. and Panigrahi, P.K. (2015) Influence of Turn Geometry on Turbulent Fluid Flow and Heat Transfer in a Stationary Two-Pass Square Duct. *International Journal of Heat and Mass Transfer*, **89**, 667-684. https://doi.org/10.1016/j.ijheatmasstransfer.2015.05.081

[19] Hunt, J.C.R., Abell, C.J., Peterka, J.A. and Woo, H. (1978) Kinematical Studies of the Flows around Free or Surface-Mounted Obstacles; Applying Topology to Flow Visualization. *Journal of Fluid Mechanics*, **86**, 179-200. https://doi.org/10.1017/s0022112078001068

[20] Tobak, M. and Peake, D.J. (1982) Topology of Three-Dimensional Separated Flows. *Annual Review of Fluid Mechanics*, **14**, 61-85. https://doi.org/10.1146/annurev.fl.14.010182.000425

[21] Perry, A.E. and Chong, M.S. (1987) A Description of Eddying Motions and Flow Patterns Using Critical-Point Concepts. *Annual Review of Fluid Mechanics*, **19**, 125-155. https://doi.org/10.1146/annurev.fl.19.010187.001013

[22] Délery, J.M. (2001) Robert Legendre and Henri Werlé: Toward the Elucidation of

Three-Dimensional Separation. *Annual Review of Fluid Mechanics*, **33**, 129-154. https://doi.org/10.1146/annurev.fluid.33.1.129

[23] Délery, J. (2013) Three-Dimensional Separated Flow Topology: Critical Points, Separation Lines and Vortical Structures. John Wiley & Sons.

[24] Liakos, A. and Malamataris, N.A. (2014) Direct Numerical Simulation of Steady State, Three Dimensional, Laminar Flow around a Wall Mounted Cube. *Physics of Fluids*, **26**, Article ID: 053603. https://doi.org/10.1063/1.4876176

[25] Syuhada, A., Hirota, M., Fujita, H., Araki, S., Yanagida, M. and Tanaka, T. (2001) Heat (Mass) Transfer in Serpentine Flow Passage with Rectangular Cross-Section. *Energy Conversion and Management*, **42**, 1867-1885. https://doi.org/10.1016/s0196-8904(01)00047-4

[26] Dukowicz, J.K. and Dvinsky, A.S. (1992) Approximate Factorization as a High Order Splitting for the Implicit Incompressible Flow Equations. *Journal of Computational Physics*, **102**, 336-347. https://doi.org/10.1016/0021-9991(92)90376-a

[27] Sheu, T.W.H. and Tsai, S.F. (2002) Flow Topology in a Steady Three-Dimensional Lid-Driven Cavity. *Computers & Fluids*, **31**, 911-934. https://doi.org/10.1016/s0045-7930(01)00083-4

[28] Chin, R.C., Vinuesa, R., Örlü, R., Cardesa, J.I., Noorani, A., Chong, M.S., *et al.* (2020) Backflow Events under the Effect of Secondary Flow of Prandtl's First Kind. *Physical Review Fluids*, **5**, Article ID: 074606. https://doi.org/10.1103/physrevfluids.5.074606

Nomenclature

N	Node
N'	Half-node
n	Connectivity of the space
p	Dimensionless pressure
Re	Reynolds number
S	Saddle
S'	Half-saddle
t	Parameter of the point on curve
$\boldsymbol{u}$	Dimensionless velocity vector
u	Dimensionless velocity component in x-axis direction
v	Dimensionless velocity component in y-axis direction
x, y, z	Dimensionless rectangular coordinate
α	The z-direction derivative of the velocity u on the surface
β	The z-direction derivative of the velocity v on the surface
μ	Viscosity
$\boldsymbol{\tau}_s$	Shear stress vector